

# A case study on the aerodynamic heating of a hypersonic vehicle

M. Mifsud

D. Estruch-Samper

D. MacManus

d.g.macmanus@cranfield.ac.uk

R. Chaplin

J. Stollery

School of Engineering  
Cranfield University  
Bedfordshire, UK

## ABSTRACT

A Parabolised Navier-Stokes (PNS) flow solver is used to predict the aerodynamic heating on the surface of a hypersonic vehicle. This case study highlights some of the main heat flux sensitivities to various conditions for a full-scale vehicle and illustrates the use of different complimentary methods in assessing the heat load for a realistic application. Different flight phases of the vehicle are considered, with freestream conditions from Mach 4 to Mach 8 across a range of altitudes. Both laminar and turbulent flows are studied, together with the effect of the isothermal wall temperature, boundary-layer transition location and body incidence. The effect of the Spalart-Allmaras and Baldwin-Lomax turbulent models on the heat transfer distributions is assessed. A rigorous assessment of the computations is conducted through both iterative and grid convergence studies and a supporting experimental investigation is performed on a 1/20th scale model of the vehicle's forebody for the validation of the numerical results. Good agreement is found between the PNS predictions, measurements and empirical methods for the vehicle forebody. The present PNS approach is shown to provide useful predictions of the heat transfer over the axisymmetric vehicle body. A highly complex flow field is predicted in the fin-body-fin region at the rear of the vehicle characterised by strong interference effects which limit the predictions over this region to a predominately qualitative level.

## NOMENCLATURE

$\alpha$	angle-of-attack, deg
$\gamma$	ratio of specific heats, $\gamma = 1.4$
$\eta$	generalised co-ordinate in the direction normal to the wall
$\mu$	dynamic viscosity, Pa·s
$\xi$	generalised co-ordinate in the direction along the wall
$\rho$	density, $\text{kg}\cdot\text{m}^{-3}$
$\varphi$	azimuth angle, deg
$c_f$	skin friction coefficient
$C_p$	pressure coefficient
$c_p$	specific heat capacity at constant pressure, $\text{J}\cdot\text{kg}^{-1}\cdot\text{K}^{-1}$
$D$	body diameter, m
$f$	functional value in Richardson's extrapolation
$h$	specific enthalpy, $\text{J}\cdot\text{kg}^{-1}$
$k$	thermal conductivity, $\text{W}\cdot\text{m}^{-1}\cdot\text{K}^{-1}$
$M$	Mach number
$n$	index in $q/q_{ref} = (p/P_{ref})^n$
$p$	static pressure, Pa
$p^*$	observed order of accuracy
$Pr$	Prandtl number, assumed = 0.72 for air
$q$	heat flux, $\text{W}\cdot\text{m}^{-2}$
$r$	recovery factor, assumed $r = 0.846$ (laminar) or $r = 0.894$ (turbulent)
$r_g$	grid refinement ratio
$R$	gas constant, $R = 287.05 \text{ J}\cdot\text{kg}^{-1}\cdot\text{K}^{-1}$ or radius, m
$Re/m$	Reynolds number per unit length, $(Re/m = \rho V/\mu)$
$St$	Stanton number, $St = q/[(\rho_\infty V_\infty c_p)(T_{aw} - T_w)]$
$T$	static temperature, $K$
$T_{aw}$	adiabatic wall temperature, $T_{aw} = T \left( 1 + r \frac{\gamma - 1}{2} M^2 \right)$
$V$	velocity, $\text{m}\cdot\text{s}^{-1}$
$x$	axial distance from leading edge, m
$y^+$	non-dimensional, sublayer-scaled wall distance

## Subscripts

$\infty$	freestream conditions
*	reference value
$Aw$	adiabatic wall
<i>coarse</i>	coarse grid
<i>e</i>	conditions at boundary-layer edge
<i>Fine</i>	fine grid
<i>Lam</i>	laminar conditions
<i>M</i>	model scale
<i>N</i>	Nose
<i>O</i>	stagnation conditions

Ref	reference value
$W$	conditions on vehicle wall
$X$	based on local values

## 1.0 INTRODUCTION

Aerodynamic heating can be critical for the integrity of hypersonic vehicles. The high kinetic energy of the air around a high-speed vehicle is converted into heat within a thin thermal layer around the body due to friction and compression, sometimes resulting in excessive surface boundary heating<sup>(1)</sup>. Accurate prediction of surface heat transfer is therefore essential in the design of vehicles operating in the hypersonic flow regime.

Computational Fluid Dynamics (CFD) simulations are today extensively used in aerospace engineering to obtain numerical predictions of the flow field. Presented in this work are numerical predictions computed using an Implicit Multigrid Parabolised Navier-Stokes (IMPNS) software<sup>(2,3)</sup>. This flow solver has been developed to offer a practical tool (rapid, robust and accurate) for problems in high-speed external aerodynamics and is based on the PNS equations, which neglect the streamwise diffusion and unsteady terms from the complete Navier-Stokes equations<sup>(4,5,6)</sup>. Consequently, the underlying PNS equations are not suitable to model unsteady flows and flows where there is an upstream influence. The aim of this work is to present an engineering case study of the heat transfer characteristics on the surface of a realistic high-speed vehicle and to study the capabilities of this computational approach. A comparison of the computational results is also made with established analytical estimates as well as with model-scale measurements.

## 2.0 HYPERSONIC VEHICLE AND OPERATING CONDITIONS

The present study is aimed at investigating the aerodynamic heating on the surface of a high-speed vehicle. The geometry is shown in Fig. 1. The forebody consists of a spherically blunt cone followed by a tangent-ogive with a length of  $2.0D$  (Fig. 2(a)). A cylindrical portion of diameter  $1.0D$  follows the nose with a length of  $16.1D$ . Four fins are located at the rear of the cylindrical body at  $90^\circ$  to each other (Fig. 2(b)), starting at  $17.086D$  from the nose tip. Five different key parts of the expected flight envelope are considered. Across these five flight phases the vehicle changes altitude and therefore the atmospheric flow conditions change as well as the flight Mach number which increases from  $M_\infty = 4$  to  $M_\infty = 8$  (Table 1). The objective of this case study is to understand the heating characteristics for the different flight phases during which it is expected that the wall

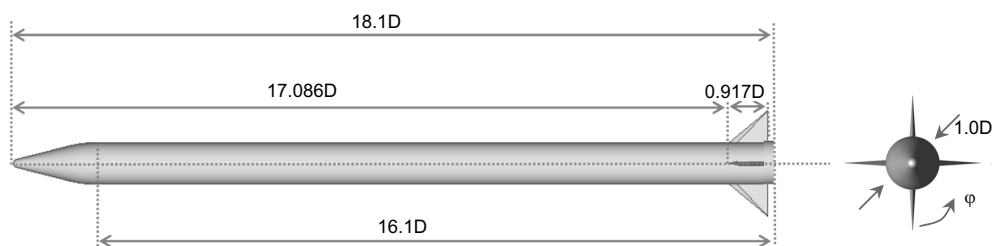


Figure 1 Full-scale hypersonic vehicle.

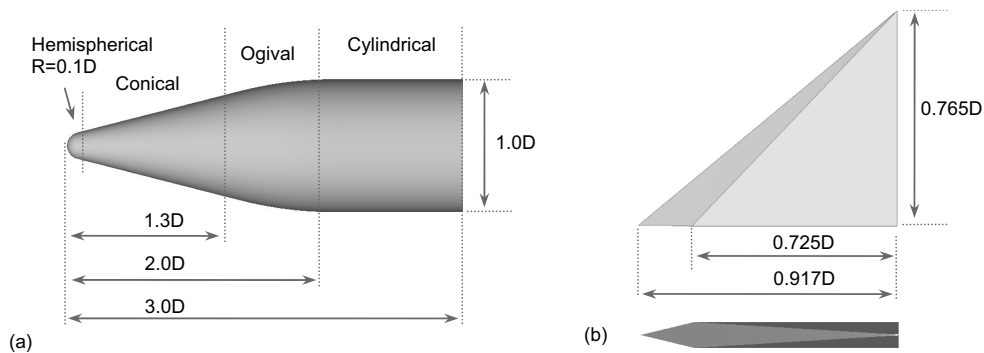


Figure 2. Hypersonic vehicle forebody (a) and fin (b) geometries.

temperature will vary. A prescribed wall temperature is imposed for each flight phase although the study also includes an assessment of the sensitivity of the heat flux to this prescribed temperature. An angle-of-attack of  $\alpha = 0^\circ$  was assumed in all cases except in those presented in Section 6, which consider the vehicle to be at  $\alpha = 2^\circ$  incidence.

**Table 1**  
**Hypersonic vehicle flight conditions**

Phase	$M_\infty$	$V_\infty$ [m·s <sup>-1</sup> ]	$T_o$ [K]	$p_\infty$ [Pa]	$\rho_\infty$ [kg·m <sup>-3</sup> ]	$T_\infty$ [K]	$T_w$ [K]	$Re_\infty/m$ [m <sup>-1</sup> ]
1	4.0	1,239	1,003	28,784	0.422	239	500	$3.37 \times 10^7$
2	5.0	1,512	1,365	22,250	0.341	227	600	$3.41 \times 10^7$
3	6.0	1,774	1,784	17,625	0.282	218	800	$3.51 \times 10^7$
4	7.0	2,028	2,255	14,225	0.237	209	800	$3.49 \times 10^7$
5	8.0	2,273	2,772	9,635	0.167	201	800	$2.85 \times 10^7$

### 3.0 IMPLICIT MULTIGRID PARABOLISED NAVIER-STOKES (IMPNS) SOLVER

The IMPNS solver provides algorithms for the solution of the Euler, thin-layer or Parabolised Navier Stokes (PNS) equations together with a range of turbulence closures. These include the algebraic model of Baldwin and Lomax<sup>(8)</sup> enhanced with modifications by either Degani and Schiff<sup>(9)</sup> or Qin and Jayatunga<sup>(10)</sup> that account for cross flow separation and variants of the one-equation model of Spalart and Allmaras<sup>(11)</sup>. The turbulence closure is coupled with the mean flow equations in a segregated fashion. The governing equations are formulated for a finite control volume and solved using an implicit space marching procedure.

For supersonic flows in which there is no upstream influence a single sweep is employed starting at the leading edge of the configuration and proceeding in the streamwise direction. The approach has also been extended to allow for flows with upstream influence, for example blunt body flows and flows exhibiting axial separation. In this case a multi-sweep procedure in which the solver marches backwards and forwards is employed to capture the elliptic characteristics of the governing equations. A combination of single sweep and multi-sweep strategies can be used to solve for flows that contain embedded regions of flow where upstream influence is important.

IMPNS provides a number of schemes that can be employed in the spatial discretisation<sup>(12)</sup>. The Steger and Warming<sup>(5)</sup> numerical scheme was used in the present study for the discretisation of both the streamwise and crossflow fluxes. This numerical scheme produces a stable space-marching scheme in the multi-sweep region capable of marching in both directions. The nominal space-wise order of accuracy in this case is 2 in the streamwise direction and 3 in the crossflow direction. An implicit system of equations arises at each marching plane following the spatial discretisation. This system is solved using a relaxation approach in which an additional pseudo-time derivative is added to the steady governing equations. The implicit system is then solved by marching to the steady state in pseudo-time. Convergence of the pseudo-time relaxation is accelerated through the use of a combination of an implicit Newton-Krylov method<sup>(13)</sup> and full multi-grid<sup>(14)</sup>.

IMPNS uses standard structured multi-block grids. To provide geometric flexibility and to reduce computational expense, non-matching block faces are permitted in the stream-wise direction. This allows changes of grid topology in the stream-wise direction, allowing the grid to be relatively easily generated while reflecting the geometric characteristics of the configuration being studied. In this work a perfect gas model was employed and real gas effects were not taken into account.

## 4.0 MODEL-SCALE INVESTIGATION

To assess the performance of the IMPNS method for hypersonic heat transfer a programme of experimental, computational and analytical investigations were first performed. An experimental study was performed on a 1/20<sup>th</sup> scale model of the vehicle's forebody in the Cranfield University gun tunnel for validation of the computational method. This configuration is evaluated using IMPNS during which the effects of grid and iterative convergence are also assessed. These experimental and computational results are also compared with the established analytical methods.

### 4.1 Model-scale conditions

The freestream Mach number in the experiments is  $M_\infty = 8.2$  and the Reynolds number per unit length  $Re_\infty/m = 9.35 \times 10^6$  (Table 2). These conditions are close to the flight conditions during phase 5, which are  $M_\infty = 8.0$  and  $Re_\infty/m = 2.85 \times 10^7$ . The total length of the scale model is  $3.0D_m$ . Measurements are made under both free transition conditions and for a more fully turbulent arrangement. For the turbulent flow a small strip of carborundum grit is placed at the junction of the spherical nose and the conical section in order to trip the laminar boundary layer to a turbulent state.

**Table 2**  
**Model scale experimental test conditions**

$M_\infty$	$\alpha [^\circ]$	$p_\infty [\text{Pa}]$	$\rho_\infty [\text{kg}\cdot\text{m}^{-3}]$	$T_\infty [\text{K}]$	$T_w [\text{K}]$	$Re_\infty/m [\text{m}^{-1}]$
8.2	0	950.3	0.0371	89.3	295	$9.35 \times 10^6$

### 4.2 Computational grid convergence study

In general, the calculation of the heat-transfer rates with a suitable accuracy is much more difficult than the calculation of the surface pressure to the same level of accuracy. This is due to the requirement for more refined grids near the surface to sufficiently capture the flow and

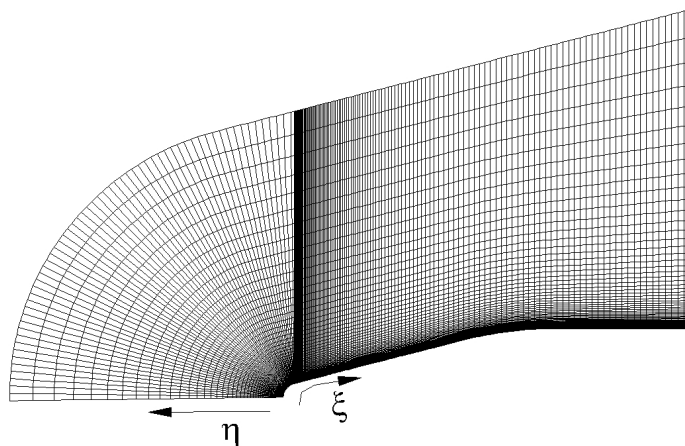


Figure 3. Axisymmetric grid points mesh of the forebody ( $181 \times 126$  for model-scale predictions).

temperature gradients which in turn also requires lower convergence criteria. Hence, to accurately represent the large velocity gradients and temperature gradients normal to the surface, it is necessary to develop suitable computational grids. Due to the inherent approximation within the boundary layer, calculations using the PNS equations require a considerable number of grid points in the boundary layer to achieve a suitable accuracy<sup>(15)</sup>. To assess the sensitivity of the predicted solutions to spatial refinement of the grid (in particular the 1<sup>st</sup> cell height and the corresponding  $y^+$  value), a grid convergence study was conducted. In performing this study it proved difficult to obtain monotonic heat flux solutions over a series of three consecutive grids with a fixed grid spacing ratio within the asymptotic range of grid convergence. However, this was obtained over two consecutive grids. From these two computations Richardson's extrapolation<sup>(16)</sup> was then used to estimate the continuum heat flux at the stagnation point.

For the model-scale predictions, a series of two-dimensional grids were generated to simulate the wind-tunnel test conditions. The grid sizes are  $181 \times 181$ ,  $181 \times 151$  and  $181 \times 126$  with a refinement ratio of 1.2 in the  $\eta$ -direction (Fig. 3). A geometric progression was used to distribute the cells in the  $\eta$ -direction, while the number of grid points in the  $\xi$ -direction was maintained constant over the series of grids after conducting a separate series of studies to ensure that it is adequate. The first wall cell distance was  $1 \times 10^{-4}$  mm,  $1.2 \times 10^{-4}$  mm and  $1.44 \times 10^{-4}$  mm for the fine, medium and coarse grids respectively. These correspond to  $y^+$  values of  $3.4 \times 10^{-3}$  and  $4.0 \times 10^{-3}$  close to the stagnation point for the fine and medium grids respectively. Such small wall cell height values are necessary as a consequence of the high Reynolds number which results in a very thin boundary-layer on the forebody. Laminar and turbulent boundary layers were simulated and an isothermal wall temperature of  $T_w = 295\text{K}$  was imposed.

For both laminar and turbulent predictions, the typical difference in the heat flux between the coarse, medium and fine grids was less than 1%. This result shows that to a practical extent, grid independent results were achieved. Consequently, the  $y^+$  values obtained from the fine grid were considered as adequate and similar scaled values were used in the other computations. To establish the stagnation point Stanton number ( $St_0$ ), a set of three consecutive grids with a fixed grid spacing ratio are considered. However a monotonic  $St_0$  distribution is not achieved within the asymptotic range of grid convergence over a series of three grids. Consequently an observed order of accuracy ( $p^*$ ) equal to the nominal order of accuracy(3) is assumed in the Richardson's extrapolation. This assumption is sensible since the grid quality in this region is reasonably good.

The Richardson's extrapolation approach<sup>(16)</sup> is used to estimate a value of a functional  $f$  at zero grid spacing which is designated as the continuum value ( $f_{h=0}$ ). This is shown in Equation (1), where  $r$  is the grid refinement ratio and  $p^*$  is the observed order of accuracy.

$$f_{h=0} \approx f_{fine} + (f_{fine} - f_{coarse}) / (r_g^{p^*} - 1) \quad \dots (1)$$

The continuum heat flux at the stagnation point is compared to that obtained using the complete Fay and Riddell formula (Equation (2))<sup>(17)</sup> for an equilibrium boundary layer with a Lewis number of unity (Table 3). Sutherland's law is used to calculate viscosity  $\mu$ . A heat flux value of  $q_o = 132.6 \text{ W/cm}^2$  at the stagnation point is evaluated for this model-scale configuration, which corresponds to a Stanton number of  $St_0 = 28.4 \times 10^{-3}$  considering laminar conditions (recovery factor,  $r = 0.846$ ) at this location.

$$q_o = 0.763(\text{Pr})^{-0.6} (\rho_e \mu_e)^{0.4} (\rho_w \mu_w)^{0.1} \left( 1/R_N (2(p_e - p_\infty)/\rho_e)^{0.5} \right)^{0.5} (h_{oe} - h_w) \quad \dots (2)$$

**Table 3**  
**Stagnation heat transfer calculations**

	<b>Medium grid</b> <b>(<math>n = 181 \times 151</math>)</b>	<b>Fine grid</b> <b>(<math>n = 181 \times 181</math>)</b>	<b>Continuum</b> <b>value</b>	<b>Analytical estimate</b> <b>(Equation (2))</b>
$St_0 (\times 10^{-3})$	29.6	28.8	27.7	28.4

The difference in evaluating  $St_0$  between the predicted continuum value and the analytical estimate is 2.5%, whereas the estimated error between the continuum value and the fine grid is 4.0%. Similar grid refinement studies are performed for the other configurations presented here and resulted in similar estimated errors. These grid independent results are for the model-scale simulations. Grid convergence analyses were also performed for the full-scale predictions and similar results were obtained. For the axisymmetric full-scale configurations the results are presented for the fine grid solutions which were  $241 \times 241$  in the  $\xi$ -direction and  $\eta$ -direction, respectively. The first wall cell distance was typically  $1.0 \times 10^{-5} \text{ mm}$ .

### 4.3 Computational iterative convergence study

Thorough iterative convergence studies were conducted for each and every computation. Considerably low values for the residual of the conservative variables were reached at each station due to the very small volume cells within the boundary layer. Typical values were  $1.0\text{e-}7$  for axisymmetric two-dimensional calculations and  $1.0\text{e-}10$  for three-dimensional cases. The effect of the station convergence criteria on the solution was examined and, for a typical example, the largest difference in Stanton number was 0.05% when the criterion was adjusted by two orders of magnitude. Similarly, over the same range in station convergence criteria, the largest change in pressure coefficient was 0.30%.

### 4.4 Model-scale measurements

Eight thin-film gauges were used for the measurement of transient temperatures on the small-scale model. These are fast response temperature-sensitive resistors which were supplied with a constant current and measure temperature changes of the order of 0.1K by monitoring the voltage across



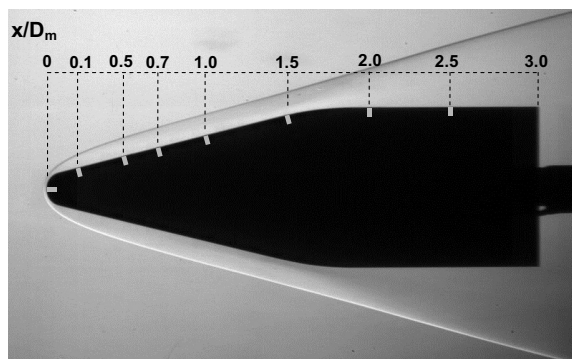


Figure 4. Schlieren image showing the symmetric flow structure as well as a schematic of the heat flux measurement locations on the model.  $M = 8.2$  and  $Re_{x/m} = 9.35 \times 10^6$ .

them. Heat flux can thus be determined with a resolution of up to  $0.1 \text{ W/cm}^2$  (i.e.  $St \approx 2 \times 10^{-5}$  in this case) using the measured time-dependent temperature and knowing the thermal properties of each gauge ( $\sqrt{\rho c k}$ ). The theory of one-dimensional heat conduction into a semi-infinite body is assumed and an analogue integrator circuit is used to determine the heat transfer as described in Ref. 18. A schlieren image is shown in Fig. 4 indicating the measurement locations along the model as well as the symmetric flow field.

A more detailed description of the experimental arrangements as well as an uncertainty analysis for this heat flux system is reported by Estruch-Samper *et al.*<sup>(19,20)</sup>. The analysis considered both systematic and random uncertainties and resulted in a total combined uncertainty of  $\pm 10\%$  in the Stanton number measurement. This is similar to the error range achieved in other similar experimental studies as reviewed by Simmons<sup>(21)</sup>.

## 4.5 Semi-empirical predictions

Whereas Fay and Riddell's method provides an estimate of the stagnation heat transfer, different semi-empirical models are also used to estimate the surface heat transfer at other locations along the forebody. The heat transfer over the conical and ogival regions of the  $1/20^{\text{th}}$  scale model for both laminar and turbulent flows are estimated using these methods as presented in the following sections.

### 4.5.1 Laminar boundary layer cases

For the laminar boundary layer cases, the approach of Crabtree *et al.*<sup>(22)</sup> is used over the conical and ogival regions of the model, i.e. at  $x/D_m = 0.2, 0.5, 0.7, 1.0$  and  $1.5$ . Considering the geometry as a hemispherically blunted cone with a semi-vertex angle of  $14.4^\circ$  ( $\approx 15^\circ$ ) and a nose radius of  $0.1D$ , the relation  $q/q_0$  is found at different points on the model based on the charts presented in their work<sup>(22)</sup>. The local heat transfer at these locations is then calculated based on the stagnation heat flux using Fay and Riddell's correlation (Equation (2)).

A different method is used to predict the laminar flow heat flux in the cylindrical part of the body, (i.e. at  $x/D = 2, 2.5$ ). The approach used in this case is Eckert's reference enthalpy method<sup>(23)</sup> which relates the heat flux to the specific heat capacity at constant pressure ( $c_p$ ), local velocity, a reference density and a driving temperature ( $T_{aw} - T_w$ ) as shown in Equation (3) and (4). The reference temperature  $T^*$  is taken as shown in Equation (5). This is subsequently used to find  $\rho^*$  using the equation of state,  $\mu^*$  is calculated from Sutherland's relation, and both are used to calculate  $Re_x^*$ .



Accurate estimates over this region can also be obtained by referring to the numerical solutions for compressible boundary layers in van Driest<sup>(1)</sup>.

$$q = \rho^* V c_p (T_{aw} - T_w) St^* \quad \dots (3)$$

$$St^* = 0.332 (Pr^*)^{-2/3} (Re_x^*)^{-1/2} \quad \dots (4)$$

$$T^* = T_e + 0.5(T_w - T_e) + 0.22(T_{aw} - T_e) \quad \dots (5)$$

#### 4.5.2 Turbulent boundary layer cases

For the turbulent boundary layer cases over the conical region, the ‘turbulent cone rule’ is assumed to obtain a similarity between the friction coefficient over the conical surface ( $c_{f,cone}$ ) with that of a flat plate ( $c_{f,plate}$ ), which is assumed as  $c_{f,cone} / c_{f,plate} \approx 1.1$  for turbulent flow<sup>(24)</sup>. Considering a sharp cone with a semi-vertex angle of  $15^\circ$ , the edge and reference conditions are obtained, with corresponding flat plate values over the conical region in this case  $M_\infty = 5.26$ ,  $p_\infty = 6,800\text{Pa}$ ,  $T_\infty = 197.4\text{K}$ <sup>(25)</sup>. The same definition of reference temperature as in Equation (5) can be used in combination with Schlichting’s<sup>(26)</sup> Reynolds analogy for turbulent flows in Equation (6). Whereas the previous approach is directly applied in the conical part, a similar method is applied over the cylindrical region but without consideration of the conical effects in this case.

$$St^* = 0.02296 / (Re_x^*)^{0.139} \quad \dots (6)$$

#### 4.6 Model-scale results

Measurements taken at different axial locations along the surface of the test model for both laminar and turbulent flows are summarised in Table 4. As expected, the measurements show the large heat transfer values at the nose followed by a generally decreasing trend moving aft on the body. Also, they show a modest increase in the heat transfer levels along the body for the turbulent case in comparison with the nominally laminar flow. The semi-empirical predictions are presented in Table 5 for both laminar and turbulent configurations. There is remarkably good agreement at the stagnation point where there is only a 1% difference between the measurements and theory. This is well within the expected accuracy of the measurement system which is estimated to be  $\pm 10\%$ . To complete the comparisons, the measurements, semi-empirical results and the IMPNS predictions are presented in Fig. 5. The laminar and turbulent recovery factors are taken as 0.846 and 0.894 respectively. The stagnation point ( $x/D_m = 0$ ) Stanton number for both cases is calculated using the laminar recovery factor.

**Table 4**  
**Model-scale measurements of Stanton number**  
**at laminar and turbulent conditions**

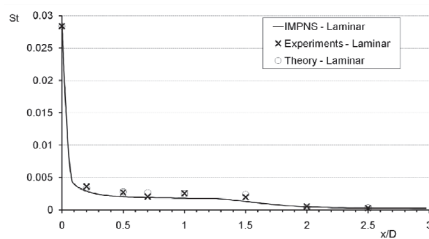
$x/D_m$	0	0.2	0.5	0.7	1.0	1.5	2.0	2.5
$St_{lam} (\times 10^{-3})$	28.4	3.6	2.7	2.1	2.6	2.0	0.6	0.3
$St_{turb} (\times 10^{-3})$	28.1	5.1	3.4	2.6	3.1	2.8	0.8	0.4

**Table 5**  
**Semi-empirical model predictions of Stanton number along the model-scale forebody under laminar and turbulent conditions**

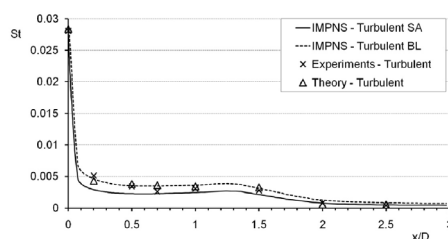
$x/D_m$	0	0.2	0.5	0.7	1.0	1.5	2.0	2.5
$St_{lam} (\times 10^{-3})$	28.4	3.4	2.8	2.7	2.5	2.4	0.4	0.3
$St_{turb} (\times 10^{-3})$	28.4	4.3	3.8	3.6	3.4	3.2	0.5	0.5

Considering the overall trend of heat flux over the forebody, the laminar predictions begin high at the stagnation point and then generally decrease over the body length. There is good agreement between the measurements and the theoretical models (Fig. 5(a)). Apart from the stagnation point where the agreement is within 1%, the IMPNS predictions generally underestimate the heat flux in comparison with the measurements. Nevertheless, the distribution along the body is similar and in absolute terms of heat flux the differences are modest.

As expected, the heat transfer increases for the turbulent configuration relative to the laminar case. On average, excluding the stagnation point, there is a 40% increase in the measured Stanton number for the turbulent case in comparison with the laminar measurements. Similar to the laminar configurations, for the turbulent case there is a peak heat transfer at the nose with a general decrease over the length of the body (Fig. 5(b)). However, both the Baldwin-Lomax (B-L) and Spalart-Allmaras (S-A) turbulent predictions show a small local heat transfer minimum at  $x/D = 0.5$  which is followed by a slight rise and then a rapid heat transfer reduction in the region where the body becomes cylindrical. In contrast, the laminar predictions show a monotonic reduction in heat transfer along the length of the body. The predictions using the algebraic turbulence model of Baldwin-Lomax predict a higher heat flux than the 1-equation turbulence model of Spalart-Allmaras (Fig. 5(b)). On average, the Spalart-Allmaras predicted Stanton number is 30% lower than that from the Baldwin-Lomax predictions. In general there is also good agreement between the measurements and the theoretical models. Over the hemisphere-cone-ogive region, both the analytical and experimental results show better agreement with the turbulent Baldwin-Lomax predictions than with the Spalart-Allmaras turbulence model. In this region the Baldwin-Lomax results are, on average, 7% higher than the measurements. In contrast, over the cylindrical portion, the Spalart-Allmaras predictions show better agreement with the measurements. In this section the Spalart-Allmaras predictions are on average 10% lower than the measurements. However, in this region the Baldwin-Lomax results are relatively high in comparison with both the measurements and the analytical results. The heat flux levels are very low and, in this aft region, the Baldwin-Lomax results are typically 45% higher than the measurements. On average over the full forebody, the difference between the measurements and the analytical values is approximately 8%. However, the measurements at  $x/D$  of 0.7 and 1.5 are consistently low relative to the analytical values and the difference is as large as 30%.



(a)



(b)

Figure 5. Computational predictions compared with experimental and theoretical predictions for (a) laminar flow and (b) turbulent flow.

## 5.0 PREDICTIONS FOR THE FULL-SCALE VEHICLE BODY

Simulations of the full scale vehicle are performed for a range of flight conditions (Table 1). Flight condition 5 ( $M_\infty = 8.0$ ,  $Re_\infty/m = 2.85 \times 10^7$ ) is used as a reference case to explore the effects of wall temperature, boundary layer transition, and transition location on the surface heat transfer. As with the previous model-scale simulations, the turbulent boundary layer is modelled using the Spalart-Allmaras and Baldwin-Lomax models.

### 5.1 Laminar and turbulent configurations

The predicted Stanton number and pressure coefficient distribution for the laminar and turbulent configurations is shown in Fig. 6(a) and (b), respectively. When the boundary layer is laminar, the surface heating is predicted to be approximately one order of magnitude lower than the turbulent conditions with only minor differences observed between the two turbulence models (Fig. 6(a)). In general, the heat flux along the cylindrical section is also one order of magnitude lower than that along the forebody for both the laminar and turbulence cases. The general distribution in the forebody region is similar to that in the model-scale experiments and predictions (Fig. 5). The laminar predictions at full-scale also show a monotonic reduction in heat transfer along the body. For the turbulent cases at full-scale, the distribution is also similar to the model-scale results with a predicted local minimum on the conical section (e.g.  $x/D \approx 0.5$  for the S-A model). Furthermore, for the turbulent Spalart-Allmaras prediction, the heat flux reaches a very modest local minimum at about  $x/D = 4.0$  and starts to increase once again with a very gentle slope beyond this point. This effect was noticed in the experimental work of Coleman and Stollery<sup>(27)</sup> and also in McWherter *et al*<sup>(28)</sup> and may be explained as a slight re-compression in the turbulent flow case, possibly due to the effective body being tapered rather than cylindrical. The laminar and turbulent models have almost no effect on the distributions of pressure coefficient (Fig. 6(b)). In all cases, the distribution shows the typical expected characteristic for this geometry. After the stagnation point there is a strong acceleration which is followed by a modest deceleration leading to the local maximum in the region of the blend point between the conical and ogival nose sections. There is a similar local minimum at the junction with the cylindrical section, after which the  $C_p$  begins to recover to the freestream values. The Baldwin-Lomax results show a spurious local minimum in the region of  $x/D = 12$ . This is discussed in the context of the range of flight conditions in section 5.4.

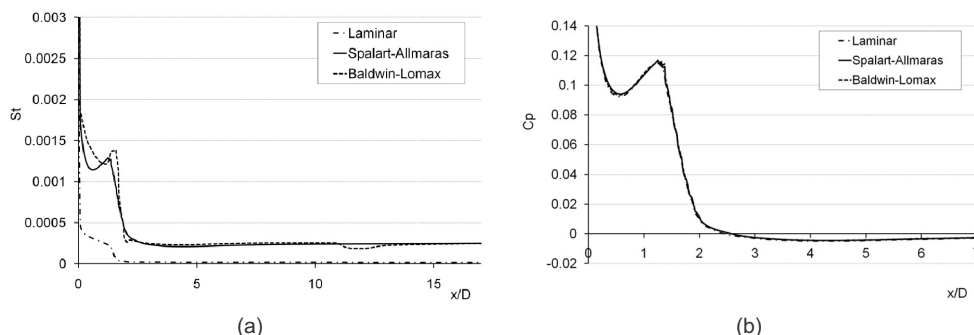


Figure 6. Computed distribution of (a) Stanton number and (b) pressure coefficient,  $C_p$ , along the axisymmetric full-scale vehicle (Flight phase 5).

## 5.2 Wall temperature effect

To evaluate the effect of wall temperature ( $T_w$ ) on the heat transfer characteristics, a set of computations were performed for flight phase 5 (Table 1) with specified wall temperatures of  $T_w = 500\text{K}$ ,  $800\text{K}$ , and  $1,100\text{K}$ . Table 6 compares the heat flux values at the stagnation point between that evaluated from Fay-Riddell's theory and the computations. In general, it is observed that the stagnation heat flux is higher at the lower temperatures. However, when this is non-dimensionalised in terms of the Stanton number, slightly lower values are found at the lower wall temperatures. The increase in the Stanton number with wall temperature is due to the changes in the gas properties near to the wall which affects the heat transfer. The variation of the heat flux value at different wall temperatures throughout the forebody is shown in Fig. 7 for laminar and turbulent conditions. The heat flux is reduced for both the laminar and turbulent configurations as the wall temperature is increased. The effect is more marked for the turbulent configurations (Fig. 7(b)).

**Table 6**  
**Theoretical and computational predictions. Flight phase 5**

$T_w(\text{K})$	Theory (Fay-Riddell)		Computations (IMPNS)	
	$q_0(\text{W/cm}^2)$	$St_0(\times 10^{-3})$	$q_0(\text{W/cm}^2)$	$St_0(\times 10^{-3})$
500	218.3	3.05	218.6	3.03
800	186.4	3.10	187.4	3.12
1,100	156.1	3.21	157.3	3.23

## 5.3 Sensitivity to transition location

In addition to the fully turbulent predictions, simulations are carried out considering different specified boundary layer transition locations. Transition locations are also imposed at the middle of the conical region ( $x/D = 0.6875$ ), and the end of the conical region ( $x/D = 1.3$ ). As expected, the heat transfer rate along the forebody is significantly lower when the boundary layer is laminar. At the transition locations, a sudden increase in the Stanton number is observed. Fig. 8 shows the comparison of the computational predictions for the different transition locations using the Spalart-Allmaras turbulence model. Similar results are observed with the Baldwin-Lomax model. Once transition occurs, the local heat transfer quickly reverts to the levels associated with the fully turbulent cases over the remainder of the body. The  $C_p$  distribution does not change.

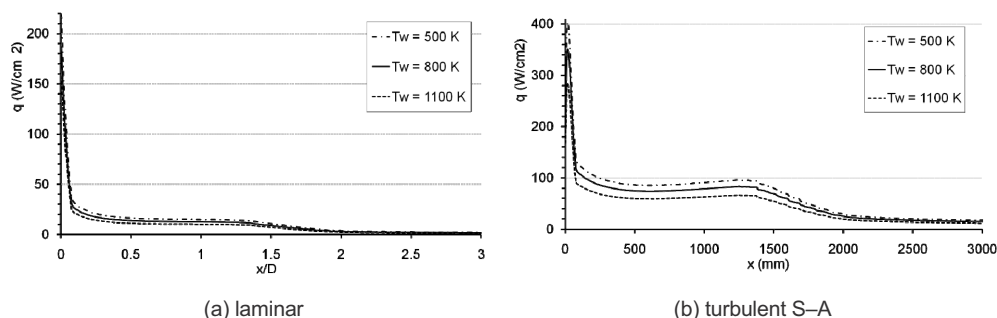


Figure 7. Heat flux per unit area along the forebody of the hypersonic vehicle at different wall temperatures: laminar case (a) and turbulent S-A case (b). Flight phase 5.

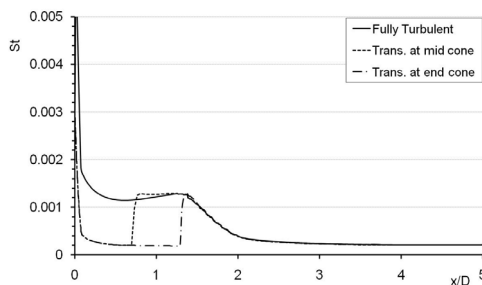


Figure 8. Stanton number along the forebody of the vehicle with different transition locations using the Spalart-Allmaras turbulence model. Flight phase 5.

#### 5.4 Effect of flight conditions

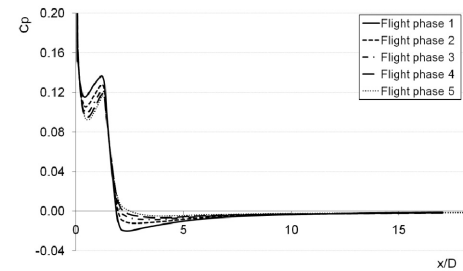
Simulations are performed at different flight conditions, in which the vehicle operates at a range of Mach numbers and altitudes. It is important to understand the characteristics of the local heat transfer effects over the flight conditions envelope investigated for the vehicle in this case study. The computed stagnation point Stanton numbers are summarised in Table 7. Overall there is good agreement between the Fay-Riddell method and the computations across all the flight conditions. It is observed that at flight phase 1 which is at Mach 4 (Table 1) the quantitative stagnation heat transfer is the lowest, and the heat flux progressively increases by a total factor of approximately 3.7 across the flight phases 2, 3 and 4. The Stanton number increases by a factor of 1.37 across the same range of flight conditions.

The distribution of heat transfer along the body also depends on the flight condition as demonstrated for laminar flow in Figs 9(a)-9(c). For the high Mach number configurations, higher heat flux is found along the vehicle. However, in non-dimensional form the Stanton number is high over the forebody region for the high Mach number cases, but it appears lower over the cylindrical portion for the same cases. This is in contrast with the trend shown by the pressure coefficient along the vehicle. The  $C_p$  is higher along the conical portion for the low Mach number cases and then starts to decrease along the ogival region until reaching negative values at the beginning of the cylindrical portion ( $x/D = 2.0$ ). Lower pressure coefficients are reached by the low Mach number cases between  $x/D = 2.0$  and  $x/D = 4.0$  and converge from  $x/D = 6.0$  to the rear of the vehicle due to the locally higher Mach numbers which eventually equalise towards  $C_p = 0$ . Therefore, as the Mach number increases higher Stanton numbers and lower pressure coefficients are found along the conical region, and in contrast lower Stanton numbers and higher pressure coefficients are found along the cylindrical portion for the high Mach number cases. Under fully turbulent conditions and using the Baldwin-Lomax model, similar comparisons are observed where the peak heat flux is predicted for Flight Phase 5 where the flight Mach number is highest at 8.0 (Fig. 10). As expected, the turbulent heat flux along the body is always much greater than the laminar values (Fig. 9) for all flight conditions.

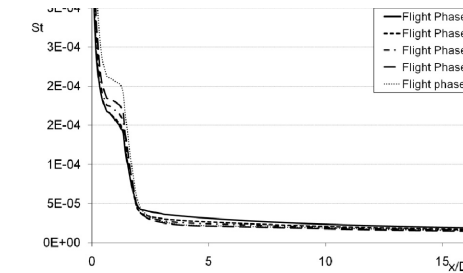
The Baldwin-Lomax model is noticed to suffer from numerical fluctuations which affect the heat transfer distributions at high wall temperature over the cylindrical portion of the body (Fig. 6(a), Fig. 10). Other flow properties such as pressure and density are not affected by similar effects when using the same turbulence model. This behaviour has already been noticed in previous studies which also highlighted the limitations of the Baldwin-Lomax model to predict surface heat transfer while a good overall agreement in the prediction of other flow features such as surface pressure and skin friction patterns was shown<sup>(29)</sup>. Due to these effects, the subsequent calculations for the finned region (Section 7) only considered results using the Spalart-Allmaras model.

Table 7  
Stagnation Stanton number predictions at different flight phases

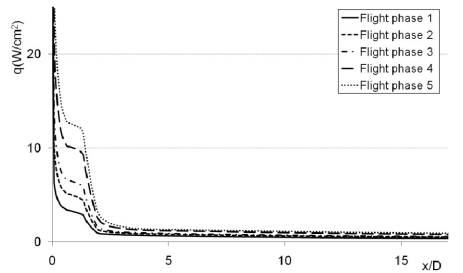
Phase	$M_\infty$	$Re_\infty/m$ ( $m^{-1}$ )	Theory (Fay-Riddell)		Laminar computations (IMPNS)	
			$q_0$ (W/cm <sup>2</sup> )	$St_0$ ( $\times 10^{-3}$ )	(W/cm <sup>2</sup> )	$St_0$ ( $\times 10^{-3}$ )
1	4.0	$3.37 \times 10^7$	38.79	1.93	39.19	1.95
2	5.0	$3.41 \times 10^7$	66.09	2.17	68.88	2.26
3	6.0	$3.51 \times 10^7$	91.78	2.46	97.86	2.62
4	7.0	$3.49 \times 10^7$	144.70	2.63	145.47	2.64
5	8.0	$2.85 \times 10^7$	186.40	3.10	187.37	3.12



(a)



(b)



(c)

Figure 9. Distributions of (a) pressure coefficient, (b) heat flux (c) Stanton number along the forebody of the vehicle at different flight conditions (Table 1). Laminar, axisymmetric predictions.

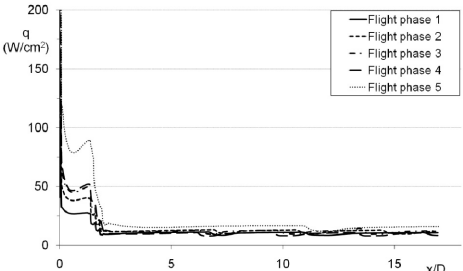


Figure 10. Distributions of heat flux along the forebody of the vehicle at different flight conditions (Table 1). Turbulent axisymmetric predictions using the Baldwin-Lomax model.

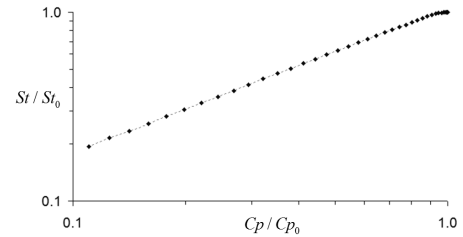


Figure 11. Sample correlation of  $St/St_0$  with  $C_p/C_{p0}$  over the hemispherical portion of the forebody at laminar conditions, showing  $n = 0.75$ .

**Table 8**  
**Values of  $n$  (from  $St/St_{ref} = (C_p/C_{p,ref})^n$ ), estimated for the**  
**hemispherical and conical portions, within  $\pm 0.05$**

Geometrical section	Laminar	Spalart-Allmaras	Baldwin-Lomax
Hemisphere ( $0 \leq x/D < 0.0751$ )	0.75	0.6	0.6
Cone ( $0.0751 \leq x/D < 1.30$ )	1.1	0.7	0.8

### 5.5 Correlation between Stanton number and pressure coefficient

A correlation between Stanton number and pressure coefficient can be expressed as  $St/St_{ref} = (C_p/C_{p,ref})^{n(30)}$ . An index,  $n$ , is determined based on the present computational results in the cases where clear correlation is possible (Table 8). This is done by plotting  $St/St_{ref}$  versus  $C_p/C_{p,ref}$  on a logarithmic scale and determining the slope of the data. The reference values ( $St_{ref}$  and  $C_{p,ref}$ ) are those found at the location where the geometrical section starts, i.e. at the stagnation point ( $x/D = 0$ ) for the correlations over the hemisphere section and at the end of the spherical section ( $x/D = 0.0751$ ) for those over the conical section. The indices are found to also depend on the turbulence models. A sample correlation is shown over the hemispherical nose with a laminar boundary layer, which shows an index of  $n = 0.75$  (Fig. 11). Good agreement is observed with previous experimental works which estimated an index of  $n = 0.72$  for a laminar boundary layer over similar hemispherical nose geometries<sup>(31)</sup>. A similar power-based correlation was not clearly established in the cylindrical region of the body.

## 6.0 PREDICTIONS FOR THE FULL-SCALE VEHICLE AT INCIDENCE

An investigation is also performed along the axisymmetric portion of the vehicle to investigate the effect of heat flux when the vehicle is at incidence. The flight conditions at phase 4 are considered ( $M_\infty = 7$ ,  $T_w = 800\text{K}$ ,  $Re_\infty/m = 3.49 \times 10^7$ ) and at an angle-of-attack of  $\alpha = 2^\circ$ . A three-dimensional domain was used with a symmetry plane along the vehicle centreline and therefore one half of the full body was modelled. Three-dimensional grids are used with a wall first-cell distance of  $1.0 \times 10^{-4}\text{mm}$  as in the previous full-scale axisymmetric cases. The grid sizes were  $241 \times 201 \times 91$  in the axial, radial and circumferential directions, respectively.

Along the forebody of the vehicle when it is at incidence, the heat flux is higher on the windward side and lower on the leeward side relative to the zero incidence configurations. For laminar flow, the heat flux on the windward side at the conical region (e.g.  $x/D = 1.0$ ) is about twice as high as this on the leeward side (Fig. 12). Further downstream, over the cylindrical region, the difference between the heat flux over both sides increases with axial location. For example, at  $x/D = 3.0$  the heat flux on the windward side is three times higher than that on the leeward side. However, at an axial location of approximately  $x/D = 5.0$ , the crossflow boundary layer separates and this ultimately results in a predicted increase in the Stanton number on the leeward side of the body (Fig. 12). The effect of the separations and re-attachments of the boundary layer along the leeward side results in a predicted complex



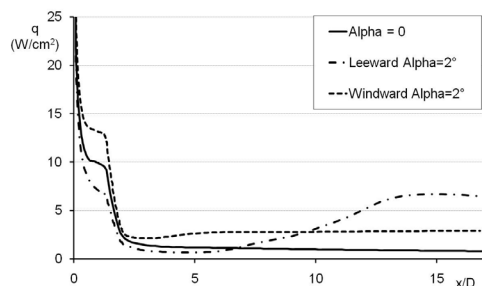


Figure 12. Heat flux distribution over leeward and windward locations compared with  $\alpha = 0^\circ$  conditions. Laminar predictions for Flight Phase 4.

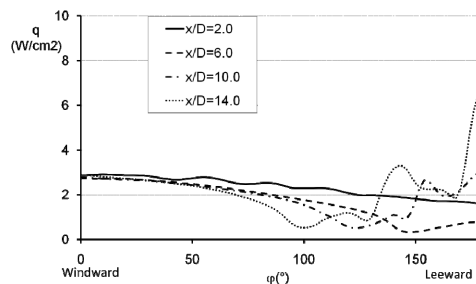


Figure 13. Calculated heat flux along the azimuth angle, corresponding to different axial locations of the vehicle. Laminar conditions, flight phase 4.

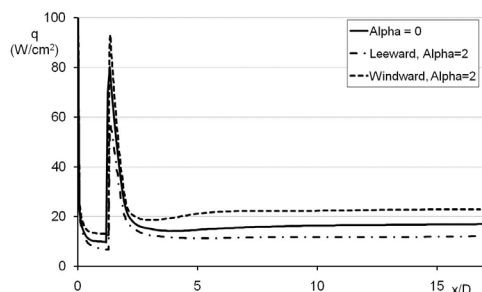


Figure 14. Heat flux distribution over leeward and windward locations compared with  $\alpha = 0^\circ$  conditions. S-A turbulent predictions for Flight Phase 4 with transition specified at the rear of the forebody conical section.

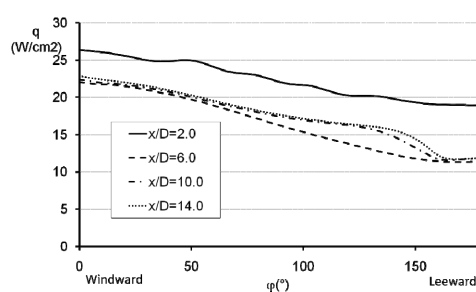


Figure 15. Calculated heat flux azimuthal distribution, corresponding to different axial locations of the vehicle. Turbulent conditions, S-A model, flight phase 4.  $\alpha = 2^\circ$ .

surface heating distribution at different axial locations of the vehicle (Fig. 13). Near the end of the body, approximately from  $x/D = 13.0$ , the leeward side has a heat flux rate approximately 2.5 higher than that on the windward side. Overall, when the vehicle is at incidence it is subject to higher aerodynamic heating than at  $\alpha = 0^\circ$  conditions except over the leeward region of the forebody where slightly reduced heat flux takes place until it separates from the surface.

However, it is well known that these slender body, crossflow-dominated features are sensitive to the state of the approaching boundary layer. Predictions were performed for a turbulent flow using the S-A model and with transition specified to occur in the adverse pressure gradient towards the end of the conical nose section at  $x/D = 1.3$ . As before (§5.3) there is a step increase in the heat flux when a turbulent boundary layer is enforced which then steeply reduces with further distance along the body on both the windward and leeward sides (Fig. 14). In comparison with the zero incidence case, as well as the characteristics on the leeward side, the windward region has a consistently higher heat flux. After the region of the local heat flux minimum which occurs at the start of the cylindrical portion, the turbulent heat flux gradually increases on both the leeward and windward sides and the heat flux on the windward side is approximately twice that on the leeward side. For the turbulent boundary layer at this modest incidence, the crossflow separation does not arise over the length of the body. Consequently, there is a relatively smooth circumferential distribution of heat flux at a range of axial locations with the peak values on the windward side (Fig. 15).

## 7.0 PREDICTIONS FOR THE FINNED REGION

Four control fins are located at the rear of the vehicle (Fig. 2). The flow field in this region is strongly three-dimensional and highly complex due to the interference induced by the fins to the incoming boundary layer. The determination of the heat transfer in such complex interactions is not well-established as yet. Consequently, to obtain useful engineering predictions, simulations are frequently used to estimate the behaviour of the flow in a qualitative manner based on other flow properties (e.g. pressure) which are not subject to the high uncertainty levels that are associated with heat transfer. Although there is substantial uncertainty on the heat transfer predictions in this region mainly due to turbulence flow modelling, gridding difficulties and the lack of experimental data by which the calculations could be validated, a range of simulations have been performed to examine the flow field and to identify the pertinent heat transfer characteristics.

The flow over the fin-body-fin region was computed using a multi-block, three-dimensional algebraic, structured grid. For PNS codes it is a requirement that grids are generated such that the planes normal to the inlet flow are at constant axial locations. An O-type topology over both streamwise blocks and wrapping the whole fin-body-fin was considered. A first wall cell distance of  $1.0 \times 10^{-4}$  mm was maintained and the cell skewness at the root and the tip of the fins was smoothed with an elliptic solver. The inlet boundary condition was determined from the axisymmetric calculations which provided the appropriate approaching boundary layer characteristics. For the turbulent calculations the approaching boundary layer ahead of the fins is relatively thick due to the growth over the long vehicle body and is  $0.22D$  thick. This is large in comparison to the fin height of  $0.765D$  and is therefore notably different from the majority of the previous work on similar geometric configurations under wind-tunnel conditions. Within the finned region alone the grid comprised 55, 121 and 181 cells in the axial, radial and circumferential directions. Both fully laminar and fully turbulent cases are considered with only the Spalart-Allmaras model being used for the turbulence configurations.

As the objective of this section is to illustrate the issues around heat transfer predictions within an engineering framework the results are only presented for the key flight condition of Flight Phase 5 (Table 1). The Stanton number distributions over the body surface between the fins and just ahead of the interaction ( $x/D = 17.21$ ) – which can be assumed as a corresponding undisturbed local heat flux – is  $St_u = 2.51 \times 10^{-4}$  and  $St_u = 1.65 \times 10^{-5}$  for the S-A and laminar conditions, respectively. As expected, the laminar value is about an order of magnitude lower than the turbulent predictions. However, as remarked in the recent literature<sup>(32)</sup>, further comparison of numerical heat flux simulations with experimental data on similar fin-body configurations (e.g. Neumann and Hayes<sup>(33)</sup>; Kussoy and Horstman<sup>(34)</sup>; Knight<sup>(35)</sup>) is restricted by the strong three-dimensionality and complexity of the local interactions and most importantly of all by the specifics of the configuration. There is a dearth of experimental data for the type of geometry considered here. The vast majority of previous research in this area has focused on idealised fins and wedges mounted on flat plates and under wind-tunnel conditions. Consequently, quantitative comparisons are hindered by the number of factors involved, which are mainly related to fin geometry (height, width, deflection, sweep, etc.) and to the freestream flow conditions (incoming boundary layer, Reynolds number, Mach number, etc.).

The present results are in broad agreement with the flow field features and heating trends found in the more detailed literature on simplified geometries (e.g. Price and Stallings<sup>(36)</sup>; Stollery<sup>(37)</sup>; Wang *et al.*<sup>(38)</sup>) – as summarised in Fig. 16. As shown in Fig. 17 and Fig. 18 for a range of selected axial locations in the laminar and Spalart-Allmaras solutions, the maximum heat transfer on the vehicle surface is found close to the fin-body junction. The Stanton number is non-dimensional

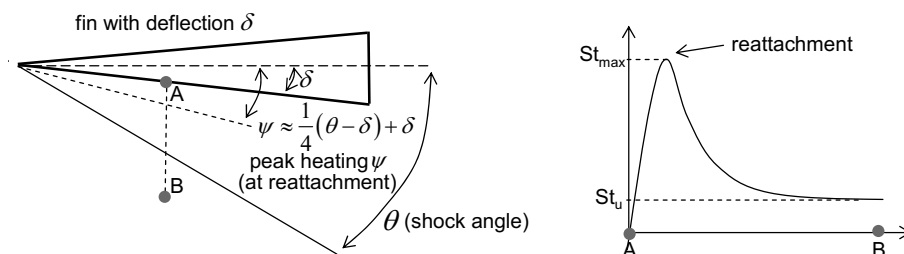


Figure 16. Schematic of flow field and field and heat flux distribution around a two dimensional wedge based on previous literature. corresponds to location of peak heat flux at each axial location.

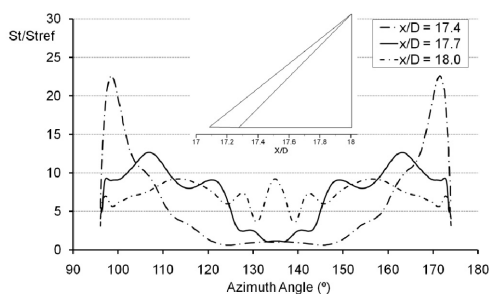


Figure 17. Variation of Stanton number with azimuth angle between the fins at different axial locations. Laminar simulations. Flight phase 4,  $\alpha = 0^\circ$ .

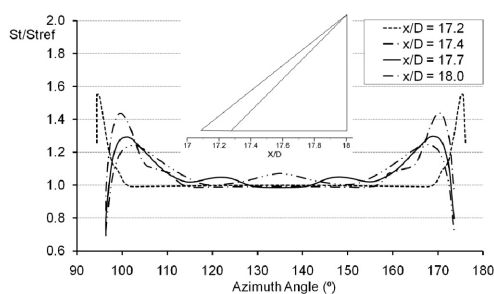


Figure 18. Variation of Stanton number with azimuth angle between the fins at different axial locations. Turbulent Spalart-Allmaras predictions. Flight phase 4,  $\alpha = 0^\circ$ .

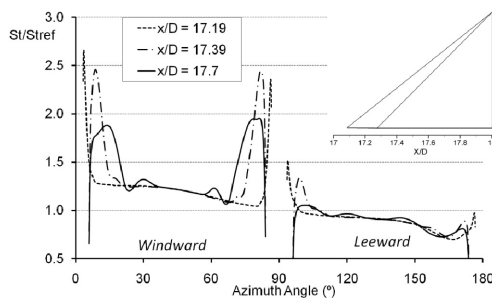


Figure 19. Variation of Stanton number with azimuth angle between the fins at different axial locations. Turbulent Spalart-Allmaras predictions. Flight phase 4,  $\alpha = 2^\circ$ .

by the appropriate local Stanton number ahead of the fins. Although the simulations also predict the heat transfer on the fin surfaces, the focus of this work is in the key part of the heat transfer augmentation on the main vehicle body. For the laminar configuration the local heat transfer is augmented by up to a factor of 22 relative to the approaching flow conditions (Fig. 17). This peak in heat transfer moves away from the fin root junction with axial distance and also reduces in magnitude. For the turbulent configuration (Fig. 18), there is also the expected local heat transfer peak which reduces in magnitude with axial distance. However, the peak local augmentation is an order or magnitude lower than for the laminar case and is lower than typical values reported

in previous research studies<sup>(35)</sup>. Key differences from previous simplified configurations are that the fin is a swept geometry with a chamfered wedge leading edge and the approaching boundary layer is substantially thicker than those studied previously. These aspects may account for some of the differences. The peak heat transfer values are not located exactly at the root of the fin but at a certain distance between the fin root and the fin shock where the flow reattaches as reported by Token<sup>(39)</sup>. In all cases, the low heat transfer near the corner and the cross-sectional heat flux characteristic distribution (e.g. A-B in Fig. 16), which increases as the distance from the corner is increased to reach a maximum and to then ultimately decrease to the undisturbed value – are qualitatively similar to those observed in more detailed experimental studies on similar configurations (Giles and Thomas<sup>(40)</sup>; Stainback and Weinstein<sup>(41)</sup>). The local heat flux reduction is expected in regions of flow separation (e.g. Neumann and Hayes<sup>(33)</sup>). Finally, the effect of the body incidence on the local heat flux distributions in the aft finned region is considered for the turbulent configurations. When the body is at  $2^\circ$  incidence, the heat transfer in the region ahead of the fins on the windward side is approximately twice as high as that on the leeward side (Fig. 14). These differences are even further accentuated in the finned region where the local heat transfer augmentation is amplified on the windward side and diminished on the leeward side. This is illustrated in Fig. 19 which shows the Stanton number distributions which are scaled to the reference Stanton number just ahead of the fins from the axisymmetric configuration and with zero incidence. At incidence, on the windward side the local heat transfer augmentation is further increased by up to 80% up to  $St/St_{ref} = 2.7$ . Furthermore, on the leeward side, the local peaks are sufficiently reduced to be generally lower than the approaching reference level (Fig. 19). Overall, this emphasises the sensitivity in the local regions of high heat transfer to small changes in the operating condition conditions and also the relatively high levels of uncertainty in predicting heat transfer for this type of flow field. It also highlights the need for new experimental data on more representative configurations beyond the existing database of predominately idealised geometries.

## 8.0 CONCLUSIONS

A case study is presented for the heat transfer over the main surface of a hypersonic air vehicle. The main engineering prediction tool is a PNS computational method which was used in conjunction with established empirical based models and experimental data. A comparison of the semi-empirical models and measurements over the forebody of a small-scale model showed close agreement with the computational results. In the turbulent cases over the hemisphere-cone-ogive region, slightly better agreement between the analytical and experimental results was observed with the turbulent Baldwin-Lomax predictions than with the Spalart-Allmaras turbulent cases. Over the cylindrical portion, however, closer agreement with the Spalart-Allmaras results was observed. For a laminar boundary layer, the heat flux is observed to be approximately one order of magnitude lower than under turbulent conditions with only minor differences between computational results using the two different turbulence models. The heat flux along the cylindrical section is also one order of magnitude lower than that along the forebody for both the laminar and turbulence cases. The sensitivity to boundary layer transition location was also assessed and calculations showed an immediate increase in heat flux as the boundary layer becomes turbulent. Once transition occurs, the local heat transfer quickly reverts to the levels associated with the fully turbulent cases over the remainder of the body. Higher heat flux values were found at lower wall temperatures but the differences are very small when considered in terms of Stanton number. Three dimensional predictions at a small angle of incidence ( $\alpha = 2^\circ$ ) showed notable differences over the forebody in comparison with the zero incidence configuration under laminar conditions. There is less

sensitivity to incidence for the turbulent configurations. Three-dimensional simulations over the aft finned region showed complex flow fields and notable augmentation in the local predicted heat flux distributions for both laminar and turbulent configurations which is amplified when the vehicle is at a small angle of incidence. In addition, it was noticed that at the physical conditions of the full-scale vehicle, the heat transfer fluctuated numerically when using the Baldwin-Lomax turbulence model at high wall temperatures. Other flow properties such as pressure and density did not suffer from similar effects. These fluctuations occurred more often as the wall temperature increased. They were not observed for the model-scale predictions.

Overall, it is shown that the performance of the present PNS code is well established for predicting the heat transfer over the axisymmetric portion of the vehicle body. However, the high complexity of the flow in the aft finned regions restricts the predictions to a qualitative level without further validation. It is highlighted that the prediction of the complex viscous interactions induced in interference regions is at present one of the main problems in high-speed aerodynamics which requires further extensive developments, both experimentally and numerically, before an accurate design prediction capability can be established for such cases. It should also be noted that even for the less complex, axisymmetric predictions very low residual levels were required to achieve iterative convergence on very fine grids. This illustrates the amount of computational effort required to achieve credible predictions.

## REFERENCES

1. VAN DRIEST, E.R. The problem of aerodynamic heating, *Aeronautical Eng Review*, October 1956, pp 26-41.
2. LUDLOW, D.K. IMPNS Theory Guide Cranfield University, 2001a, CoA Report NFP-0112.
3. LUDLOW, D.K. IMPNS User's Manual Cranfield University, 2001b, CoA Report NFP-0113.
4. VIGNERON, Y.C., RAKICH, J.V. and TANNEHILL, J.C. Calculation of supersonic viscous flows over delta wings with sharp leading edges, 1978, AIAA Paper 78-1137.
5. STEGER, J.L. and WARMING, R.F. Flux vector splitting of the Inviscid gas-dynamic equations with applications to finite difference methods, *J Computational Physics*, 1981, **40**, pp 263-293.
6. BIRCH, T., QIN, N. and JIN, X. Computation of supersonic viscous flows around a slender body at incidence, 1994, AIAA Paper 94-1938.
7. BIRCH, T., PRINCE, S., LUDLOW, D. and QIN, N. The application of a parabolized Navier-Stokes solver to some hypersonic flow problems, 2001, AIAA Paper 2001-1753.
8. BALDWIN, B. and LOMAX, H. Thin Layer approximation and algebraic model for separated turbulent flow, 1978, AIAA Paper 78-257.
9. DEGANI, D. and SCHIFF, L.B. Computation of turbulent supersonic flows around pointed bodies having cross-flow separation, *J Computational Phys*, 1986, **66**, (3), pp 173-196.
10. QIN, N. and JAYATUNGA, C. Algebraic Turbulence Modelling for Vortical Flows Around Slender Bodies, 1998, NATO RTO-MP-5, Missile Aerodynamics.
11. SPALART, P.R. and ALLMARAS, S.R. A One-Equation Turbulence Model for Aerodynamic Flow, 1992, AIAA Paper 92-0439.
12. QIN, N. and LUDLOW, D.K. A cure for anomalies of Osher and AUSM+ schemes for hypersonic viscous flows around swept cylinders, in Proceedings of the 22nd International Symposium on Shock Waves, Imperial College, London, UK, July 18-23 1999, (Eds: BALL, G.J., HILLIER, R. and ROBERTS, G.T.), pp 635-640.
13. SHAW, S. and QIN, N. A matrix-free preconditioned Krylov subspace method for the PNS equations, 1998 AIAA Paper 98-111.
14. QIN, N., LUDLOW, D.K., ZHONG, B., SHAW, S. and BIRCH T.J. Multigrid acceleration of a preconditioned GMRES implicit PNS solver, 1999, AIAA Paper 99-0779.
15. STETSON, K.F. Hypersonic boundary-layer transition, pp 324-417, in: *Advances in Hypersonics*, Volume 1: Defining the Hypersonic Environment, 1992, BERTIN, J.J., GLOWINSKI, R. and PERIAUX, J., Birkhauser, Boston, MA, USA.

16. ROACHE, P.J. *Verification and Validation in Computational Science and Engineering*, 1998, Hermosa Publishers.
17. FAY, J.A. and RIDDELL, F.R. Theory of Stagnation Point Heat Transfer in Dissociated Air, *J Aeronautical Sciences*, 1958, **25**, (2), pp 73-85.
18. SCHULTZ, D.L. and JONES, T.V. Heat-transfer measurements in short-duration hypersonic facilities, 1973, AGARD-AG-165.
19. ESTRUCH-SAMPER, D., MACMANUS, D.G. STOLLERY, J.L., LAWSON N.J. and GARRY, K.P. Hypersonic interference heating in the vicinity of surface protuberances, *Experiments in Fluids*, 2010, **49**, (3), pp 683-69.
20. ESTRUCH-SAMPER, D. Hypersonic Interference Aerothermodynamics, PhD Thesis, 2009, Cranfield University.
21. SIMMONS, J. Measurement techniques in high-enthalpy hypersonic facilities, *Exp. Thermal Fluid Science*, 1995, **10**, (4), pp 454-469.
22. CRABTREE, L.F., DOMMETT, R.L. and WOODLEY, J.G. Estimation of Heat Transfer to Flat Plates, Cones and Blunt Bodies, Royal Aircraft Establishment TR No. 65137.
23. ECKERT, E.R.G. Engineering relations for friction and heat transfer to surface in high velocity flow, *J Aeronautical Sciences*, 1955, **22**, (8), pp 585-587.
24. WHITE, F. *Viscous Fluid Flow*, 2005, McGraw Hill, 3rd ed.
25. NACA, Equations, tables and charts for compressible flow, 1953 NACA report 1135.
26. SCHLICHTING, H. *Boundary Layer Theory*, 1979, 7th ed. McGraw-Hill, NY, USA.
27. COLEMAN, G.T. and STOLLERY, J.L. A Study of Hypersonic Boundary Layers Over a Family of Axisymmetric Bodies at Zero Incidence: Preliminary Report and Data Tabulation, 1973, Imperial College of Science and Technology, England, I.C. Aero. Report 73-06.
28. McWHERTER, M., NOACK, R.W. and OBERKAMPE, W.L. Evaluation of Boundary-Layer and Parabolized Navier-Stokes Solutions for Re-entry Vehicles, *J Spacecrafts and Rockets*, 1986, **23**, (1), pp 70-78.
29. NARAYANSWAMI, N., KNIGHT, D.D. and HORSTMAN, C.C. Investigation of a hypersonic crossing shock wave/turbulent boundary layer interaction, *J Shock Waves*, 1993, **3**, (1), pp 35-48.
30. HAYES, J.R. and NEUMANN, R.D. Introduction to the Aerodynamic Heating Analysis of Supersonic Missiles, 1992, AIAA Publishing, Washington DC, USA.
31. Kemp, H., Rose, P., Detra, R., Laminar Heat Transfer Around Blunt Bodies in dissociated air, *J Aerospace Sciences*, 1959, **26**, pp 421-430.
32. BERTIN, J. and CUMMINGS, R. Critical hypersonic aerothermodynamic phenomena, *Annual Rev Fluid Mech*, 2006, **38**, pp 129-157.
33. NEUMANN, R.D. and HAYES, J.R. Aerodynamic heating in the fin interaction region of generalized missile shapes at Mach 6 (Modular missile test program), 1979, AFFDL-TR-79-3066.
34. KUSSOY, M.I. and HORSTMAN, K.C. Intersection shock-wave/turbulent boundary-layer interactions at Mach 8.3, 1992, NASA TM 103909.
35. KNIGHT, D. Numerical Simulation of 3-D Shock Wave Turbulent Boundary Layer Interactions, 1993, AGARD Report 792.
36. PRICE, E.A. and STALLINGS, R.L. Investigation of turbulent separated flows in the vicinity of fin-type protuberances at supersonic Mach numbers, 1967 NASA TN D-3804.
37. STOLLERY, J.L. A Special Course on Three-Dimensional Supersonic/Hypersonic Flows including separation, 1989, AGARD Report No. 764.
38. WANG, S.F., REN, Z.Y. and WANG, Y. Effects of Mach number on turbulent separation behaviours induced by blunt fin. *Exp Fluids*, 1998, **25**, (4), pp 347-351.
39. TOKEN, K.H. Heat transfer due to shock wave turbulent boundary layer interactions on high speed weapon systems, 1974 AFFDL-TR-74-77.
40. GILES, H.L. and THOMAS, J.W. Analysis of hypersonic pressure and heat transfer tests on a flat plate with a flap and a delta wing with body, elevons, fins, and rudders, 1966, NASA CR-536.
41. STAINBACK, P.C. and WEINSTEIN, L.M. Aerodynamic heating in the vicinity of corners at hypersonic speeds, 1967, NASA TN D-4130.

# A case study on the aerodynamic heating of a hypersonic vehicle

Mifsud, Michael

2012-09-30T00:00:00Z

---

M. Mifsud, D. Estruch-Samper, D. MacManus, R. Chaplin, J. Stollery, A case study on the aerodynamic heating of a hypersonic vehicle, The Aeronautical Journal, Volume 116, Issue 1183, Pages 873-893.

<http://dspace.lib.cranfield.ac.uk/handle/1826/8157>

*Downloaded from CERES Research Repository, Cranfield University*